Fu *et al. Biochar* (2024) 6:77
https://doi.org/10.1007/s42773-024-00373-8

Biochar

ORIGINAL RESEARCH

Open Access

Novel utilization exploration for the dephosphorization waste of Ca–modified biochar: enhanced removal of heavy metal ions from water

Weilin Fu[1,2†], Mengmeng Li[1,2†], Hongan Chen[1,3], Jianhua Qu[4], Lisheng Zhang[1,2], Shangkai Qiu[1,2], Menghan Feng[1,2], Mingyao Yuan[1,2], Changbin Guo[1,2], Jien Zhou[1,2], Zhaolin Du[1,3*] and Feng Wang[1,2*]

Abstract

Phosphorus-modified biochar has been proven to enhance the precipitation and complexation of heavy metal ions from wastewater. However, the current modification methods require large amounts of exogenous P and have high energy consumption. Hence, this study proposes and analyzes a strategy integrating biochar production, phosphorus wastewater treatment, dephosphorization waste recovery, and heavy metal removal. "BC-Ca-P" was derived from Ca-modified biochar after phosphorus wastewater treatment. The adsorption of Pb(II) by BC-Ca-P followed the Langmuir isotherm and pseudo–second–order kinetic models. The maximum adsorption capability of 361.20 $mg{\cdot}g^{-1}$ at pH 5.0 for 2 h was markedly greater than that of external phosphorous-modified biochar. The adsorption mechanisms were dominated by chemical precipitation and complexation. Furthermore, density functional theory calculations indicated that oxygen-containing functional groups (P-O and C-O) contributed the most to the efficient adsorption of Pb(II) onto BC-Ca-P. To explore its practical feasibility, the adsorption performance of BC-Ca-P recovered from an actual environment was evaluated. The continuous-flow adsorption behavior was investigated and well-fitted utilizing the Thomas and Yoon–Nelson models. There was a negligible P leakage risk of BC-Ca-P during heavy metal treatment. This study describes a novel and sustainable method to utilize dephosphorization waste for heavy metal removal.

Handling editor: Wenfu Chen

†Weilin Fu and Mengmeng Li contributed equally to this work.

*Correspondence:
Zhaolin Du
duzhaolin@caas.cn
Feng Wang
wangfeng_530@163.com
Full list of author information is available at the end of the article

Article Highlights

- Dephosphorization biochar waste was used to sustainably remove heavy metals from wastewater.
- Field-recovered dephosphorization biochar waste displayed high Pb adsorption capacity.
- Dephosphorization biochar for heavy metal removal is an eco–friendly waste–reduction and resource–utilization method.

Keywords Ca-modified biochar, Dephosphorization, Waste recovery, Heavy metal removal, Density functional theory calculation

Graphical Abstract

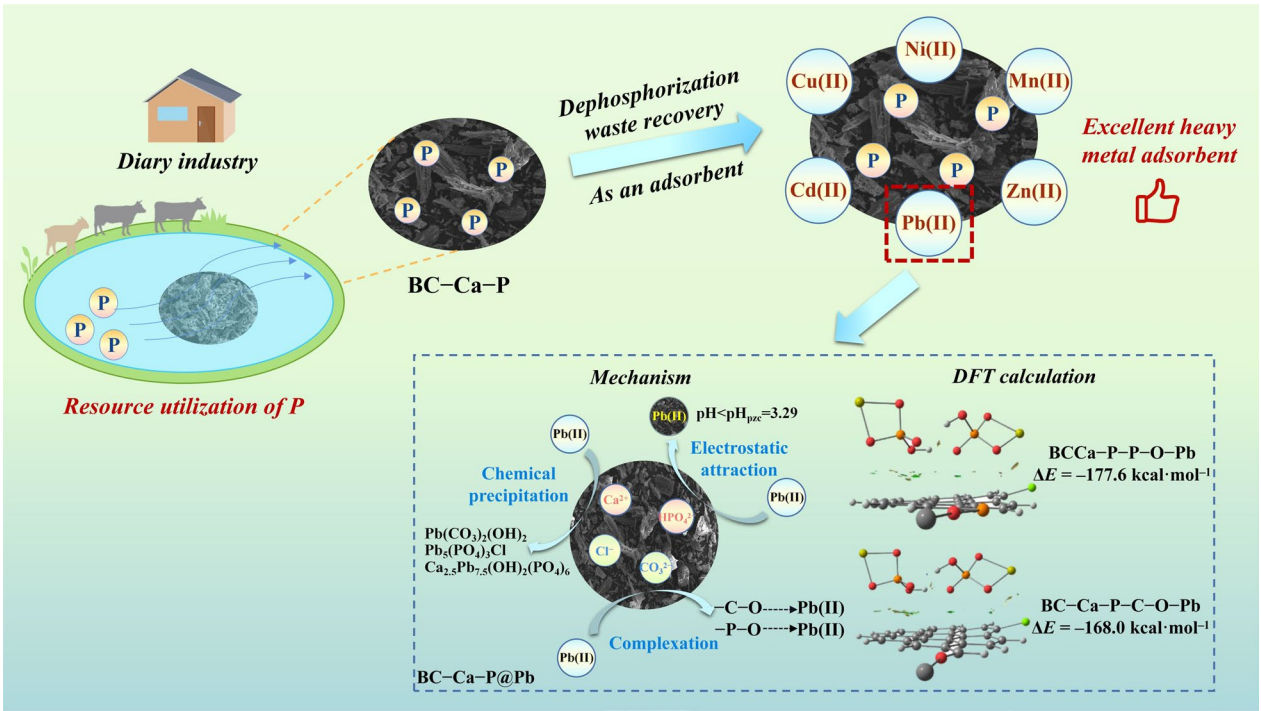

1 Introduction

Large amounts of heavy metals, inciuding lead, manganese, nickel, zinc, cadmium, and copper, have been discharged due to the rapid rise of industrial activities, damaging soil and water habitats. Even at extremely low concentrations, these harmful and non-biodegradable contaminants pose a threat to human health by contaminating the food chain and accumulating over time (Du et al. 2016; Karunaratne et al. 2022; Qu et al. 2023b). There needs to be a solution to this heavy metal pollution catastrophe.

Current methods for heavy metal wastewater treatment contain chemical precipitation (Xu et al. 2021b), bioremediation (Zhu et al. 2024), and adsorption (Yun et al. 2022; Liu et al. 2023a). Due to its great efficacy and simplicity of operation, adsorption is frequently utilized to eliminate heavy metal ions from water (Du et al. 2021; Dong et al. 2022; Zhai et al. 2023). Biochar is currently considered one of the most promising adsorbents because of its affordability, abundant raw materials, and environmental friendliness (Qu et al. 2022; He et al. 2022; Li et al. 2022b). Biochar is often prepared by the pyrolysis of agricultural and forestry wastes and has distinctive physicochemical features. The surface of biochar exhibits electronegativity, which facilitates its electrostatic attraction with heavy metal ions during adsorption, thereby

promoting adsorption efficiency. In addition, the degree of aromatization of biochar increases with the increase of pyrolysis temperature, thereby enhancing its adsorption capacity for heavy metal ions (Xia et al. 2021; Wang et al. 2022). Unfortunately, the adsorption capacity of virgin biochar for pollutants is limited. Yuan et al. (2020) and Ma et al. (2014) prepared virgin biochar for adsorbing Cd and Cr(VI), respectively, with adsorption capacity of only 24.77 $mg{\cdot}g^{-1}$ and 23.09 $mg{\cdot}g^{-1}$. This is because virgin biochar generally possesses limited specific surface area and few functional groups, leading to poor adsorption performance (Qiu et al. 2022a).

Lately, biochar modification, which substantially improves surface properties for the enhanced adsorption of heavy metals, has received increasing interest (Chen et al. 2022b, 2022a; Liu et al. 2022). Phosphorus-modified biochar possesses numerous P-containing functional groups that can enhance the precipitation and complexation of heavy metal ions (Yang et al. 2021). For example, Xu et al. (2021a) used KH_2PO_4-modified sawdust biochar, increasing the Pb(II) adsorption capability to 154.7 $mg{\cdot}g^{-1}$, six-times that of the original biochar. However, P is an important nonrenewable resource. Global P reserve shortages and increases in demand have increased costs, and the current biochar P-modification methods require large amounts of exogenous P, with high energy consumption, which is incompatible with the development of green, environmentally friendly, and low-carbon-footprint materials.

The biochar used to remove P from wastewater may be an effective solution to this problem (Luo et al. 2024). Excess P in aqueous environments (e.g., aquaculture wastewater) can easily cause water eutrophication and endanger ecosystem balance. When it comes to efficiently removing P from water, biochar shows great promise. However, disposing of dephosphorization waste properly is a challenge. Generally, biochar dephosphorization waste is used as a slow-or controlled-release fertilizer in soils, improving soil fertility and productivity (Wang et al. 2021; Marcińczyk and Oleszczuk 2022; Jia et al. 2023; Liu et al. 2023b). However, few studies have focused on the heavy-metal-removal potential of biochar dephosphorization waste. In a previous study, Feng et al. (2022a) used calcium-modified biochar (Ca-BC) prepared from oyster shells and tobacco stalks to adsorb phosphate with an adsorption capacity of up to 93–96 mg $P{\cdot}g^{-1}$. Chemical precipitation is the main mechanism of P removal from water by Ca-modified biochar. The surface pore expansion and the increase of organic functional groups during the loading process also contributed to the improvement of its phosphate adsorption capacity. In addition, it took only 5 h for Ca-BC to reach adsorption equilibrium. It thus can be seen that Ca-modified biochar shows good phosphate adsorption capacity. Following dephosphorization, the quantity of surface P-containing functional groups on Ca-modified biochar increased due to the significant binding affinity between calcium and phosphate (Almanassra et al. 2021). Unlike other commercial adsorbents, Ca-modified biochar can be derived from low-cost waste tobacco stalk. The dephosphorization cost can be sharply decreased, increasing economic attractiveness and competitiveness. Therefore, it may be possible to use biochar dephosphorization waste as a heavy metal adsorbent, eliminating the need for external phosphate and simultaneously managing dephosphorization waste.

In this work, Ca-modified tobacco stalk biochar was utilized after dephosphorization to remove heavy metals from water. This study aimed to (1) systematically compare the heavy-metal-removal performance of Ca-modified biochar dephosphorization waste and exogenous P-modified biochar, (2) comprehensively characterize the surface morphology and chemical properties of the materials, (3) investigate the potential adsorption mechanisms involved in the uptake of Pb(II) onto the Ca-modified biochar dephosphorization waste, and (4) investigate the practical application of heavy metal removal using Ca-modified biochar dephosphorization waste.

2 Materials and methods

2.1 Biochar preparation and modification

2.1.1 Preparation of biochar (BC)

Tobacco stalks were obtained from a tobacco plot in Dali City, Yunnan Province, China. Supplementary material Text S1 contains information about chemical reagents and material source. Tobacco stalk powder was heated in a muffle furnace for 2 h at 500–700 ℃. The temperature rise rate was controlled at 5–10 $℃{\cdot}min^{-1}$. After the reaction, the product underwent two rounds of washing with deionized water, followed by drying at 105 °C until a constant weight was achieved. Subsequently, it was ground and sieved through a 60-mesh sieve. The result was termed 'BC.'

2.1.2 Preparation of modified BC by exogenous P addition

The biochar was modified using an impregnation method. Biochar (2.0 g) was added to a conical flask with 300 mL of KH_2PO_4 solution (1000 mg $P{\cdot}L^{-1}$). The flask was shaken for 24 h at 25 °C and 180 rpm (default temperature and rotational speed were used unless otherwise specified). After the reaction, the subsequent steps were as described in Sect. 2.1.1. The resulting P-modified biochar was termed 'BC-P'.

2.1.3 Preparation of modified BC by dephosphorization waste recovery

First, BC-Ca was obtained as follows: BC (10.0 g) was introduced into a conical flask containing 100 mL of $CaCl_2$ solution (0.5 mol·L^{-1}) and shaken for 48 h. Second, BC-Ca-P was prepared, as follows: BC-Ca (2.0 g) was added to a conical flask with 300 mL of KH_2PO_4 solution (1000 mg P·L^{-1}; KH_2PO_4 solution was used as a simulated P-containing wastewater for this experiment) and the flask shaken for 24 h. After the reaction, the subsequent steps were as described in Sect. 2.1.1.

2.2 Characterization technique and batch adsorption process

The surface morphology, pore structure, functional group changes, diffraction patterns, element chemical states and zeta potential of adsorbents were characterized, with detailed information provided in Supplementary Material Text S2. The isothermal adsorption, adsorption kinetics, pH influence, and selective adsorption studies are covered in detail in Supplementary Material Text S3.

2.3 Computation of density functional theory

The geometry of the adsorbents was optimized using the M06–L functional corrected with the Grimme dispersion (D3) (Grimme et al. 2010) and density functional theory (DFT). GaussView 6.1 was utilized to display the optimized geometries. The 6–31G (d,p) basis set was utilized for C, H, O, P, and Cl atoms, whereas the SDD basis set was employed to Ca and Pb atoms. All geometric optimization calculations were performed using Gaussian 16. Noncovalent interaction (NCI) (Contreras-García et al. 2011) indices were employed to understand the weak adsorption interactions on the ground of the quantum theory of atoms in molecules using Multiwfn software (Lu and Chen 2012). The complex's interaction energy (ΔE) was computed as the subtracting difference between its total energy and the sum of its components' energies.

2.4 Practical application process investigation

2.4.1 Adsorption by dephosphorization waste recovered from the field

Real P-containing wastewater from the Livestock Cultivation Industry (Dali City, Yunnan Province, China)

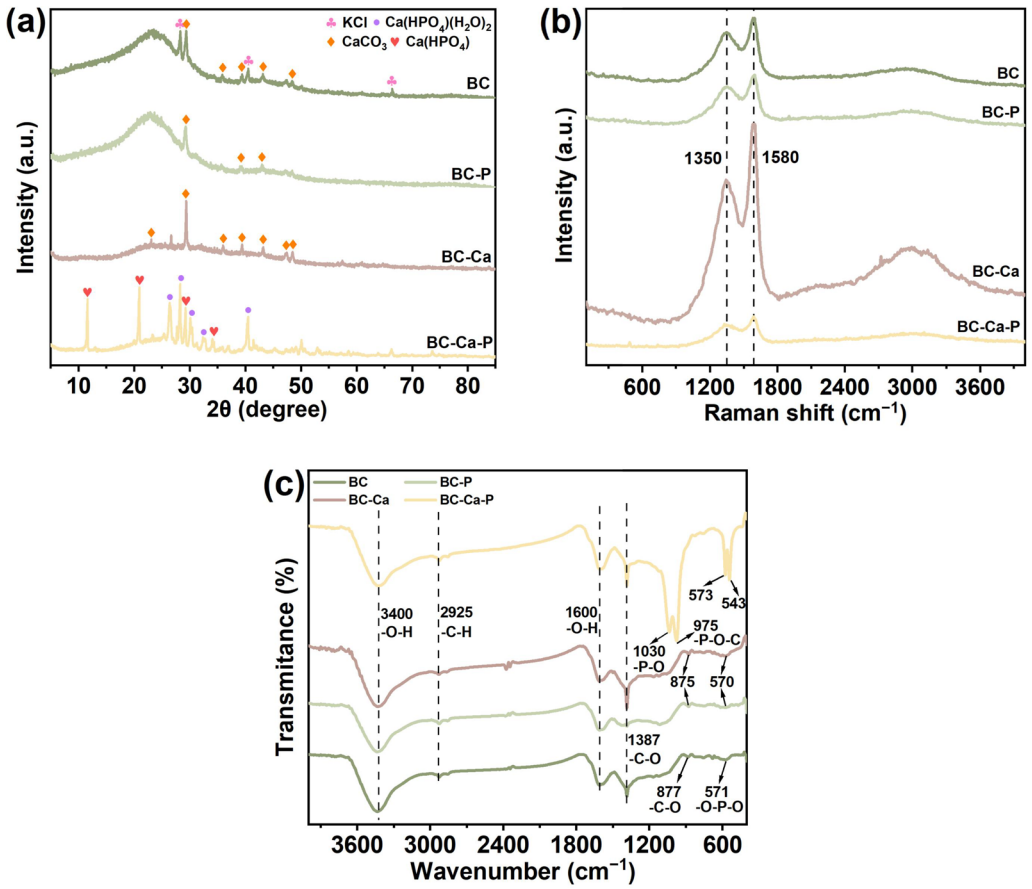

Fig. 1 **a** XRD patterns; **b** Raman spectra; **c** FTIR spectra of BC, BC-P, BC-Ca, and BC-Ca-P

was used to research the Pb(II) adsorption performance of dephosphorization waste. The concentration of total phosphorus was measured to be 63.79 ± 2.5 mg $P{\cdot}L^{-1}$ (KH_2PO_4), while the wastewater pH was recorded as 7.53. In total, 100 mL of real wastewater was placed in a flask with 0.1 g of BC-Ca for 24 h of adsorption, and another 100 mL of BC was added as a control. After the reaction, the adsorbents were recovered and added (0.4 $g{\cdot}L^{-1}$) to conical flasks containing $Pb(NO_3)_2$ solution (200 $mg{\cdot}L^{-1}$, pH of 5.0), as detailed in Sect. 2.4.1.

2.4.2 Continuous-flow adsorption process

Continuous-flow adsorption was performed in an adsorption column with an inner diameter of 10 mm and height of 15 cm. The BC-Ca-P dosage was set at 0.5 g, and the flow velocity of the $Pb(NO_3)_2$ solution (400 $mg{\cdot}L^{-1}$, pH of 5.0) was adjusted by a peristaltic pump to 2 $mL{\cdot}min^{-1}$. The Pb(II) content (C_t) in the wastewater was determined at regular intervals using flame atomic spectrometry. To determine the Pb(II) removal performance of the different adsorbents, breakthrough curves were plotted using C_t/C_0 as a function of time.

2.4.3 Phosphorus Leaching Test

BC-Ca-P (0.4 $g{\cdot}L^{-1}$) was added to conical flasks containing $Pb(NO_3)_2$ solution and deionized water. At 25 °C, the flask was shaken for 24 h at 180 rpm. Following the reaction, 0.45-μm microporous membrane filters were used to filter the solution, and the P concentration of the filtrate was detected at a wavelength of 700 nm using ultraviolet spectrophotometry (TU–1810D, CN).

3 Results and discussion

3.1 Structure and chemical composition analysis of BC, BC-P, and BC-Ca-P

The BC exhibited a traditional biochar structure and morphology (Online Resource Fig. S1, Table S1). Compared with BC, BC-P had a more granular structure due to the P coating on the surface (P increased from 0.30% to 0.45%). BC-Ca had a rougher surface than BC, possibly due to $CaCl_2$ impregnation and the appearance of irregular precipitation of $CaCO_3$ on the biochar's surface (Ca and Cl increased by 5.91% and 10.36%, respectively) (Feng et al. 2022a). After P adsorption onto BC-Ca, BC-Ca-P had a comparatively smooth surface. Notably, the percentage of P was seven times greater than that of BC-P, suggesting that the higher Ca concentration of BC-Ca-P fixed more P due to its stronger binding ability (He et al. 2020; Cao et al. 2020). The surface distribution of P was essentially the same as that of Ca according to the EDS spectra of BC-Ca-P.

The results of pore structure analysis for each biochar sample are presented in Online Resource Table S1. Compared with BC, the specific surface area (SSA), total pore volume (TPV), and average pore size (APS) of BC-P were not significantly changed. However, the SSA and TPV of BC-Ca decreased to 9.08 $m^2{\cdot}g^{-1}$ and 0.028 $cm^3{\cdot}g^{-1}$, respectively, while the average pore size increased to 12.17 nm. This phenomenon was attributed to the attachment of modified substances, which blocked some pores, especially micropores (Fan et al. 2020). Therefore, BC-Ca had decreased SSA and TPV compared to BC, and an increase in the proportion of mesopores and macropores increased the average pore size. After phosphate adsorption by BC-Ca, the SSA, TPV, and APS decreased slightly.

Figure 1a shows that some small diffraction peaks of $CaCO_3$ (PDF#97–004–0545) and KCl (PDF#97–002–2156) were detected in BC. After P adsorption, the KCl diffraction peaks disappeared for BC-P, and no other P diffraction peaks appeared, suggesting that phosphate was absorbed via ion exchange. However, the intensity of the $CaCO_3$ diffraction peaks increased after loading with Ca, indicating that Cl^- exchanged with P and Ca was loaded onto the biochar surface as $CaCO_3$. The main

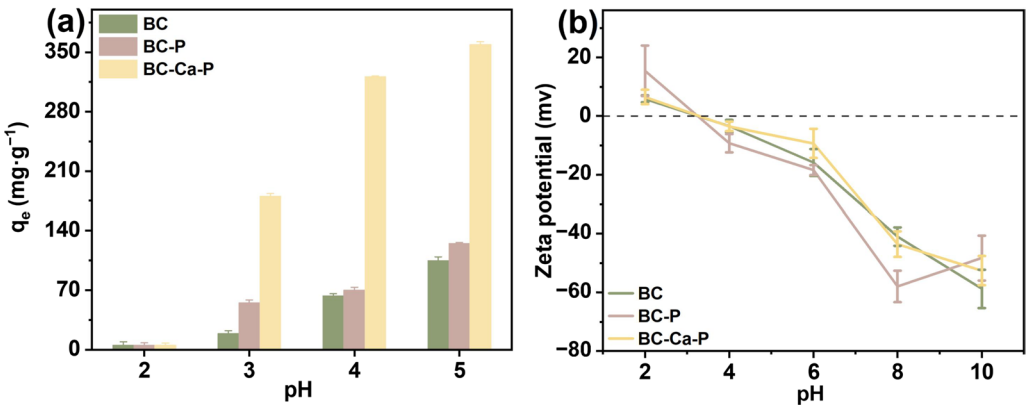

Fig. 2 Influence of initial pH on **a** Pb(II) adsorption and **b** zeta potential of BC, BC-P, and BC-Ca-P

diffraction peaks of BC-Ca-P belonged to $Ca(HPO_4)$ (PDF#97–003–8128) and $Ca(HPO_4)(H_2O)_2$ (PDF#97–001–6738) (Tan et al. 2021).

Figure 1b shows two distinct scattering peaks (1350 and 1580 cm^{-1} for the D and G peaks, respectively). The D peak indicates the defect level of the carbon structure and the extent of disorder of amorphous carbon, whereas the G peak reflects the graphitization degree of the carbon structure, attributable to vibrational patterns within the graphite plane (Feng et al. 2022b; Cao et al. 2023). Therefore, changes in defect level could be measured as the ratio of the D and G peaks (I_D/I_G). BC-Ca had a lower I_D/I_G value (0.90) than BC (0.96), indicating a defect level decrease after Ca modification, possibly due to $CaCO_3$ precipitation, which occupied some surface defects. However, the I_D/I_G values of BC-P (0.97) and BC-Ca-P (0.98) were higher than those of BC and BC-Ca, demonstrating that defect levels increased with increasing P concentration. Therefore, the addition of P may destroy the carbon structure and create defects.

Figure 1c reveals that the-OH stretching vibration was related to the peaks at 3400 and 1600 cm^{-1} (Zhang et al. 2021); the C–H stretching vibration in biochar was related

Table 1 Pseudo–first–order, pseudo–second–order and intraparticle diffusion model parameters of BC, BC-P, and BC-Ca-P

Models	Parameters	Materials		
		BC	BC-P	BC-Ca-P
Pseudo–first–order	K_1 (min^{-1})	0.0032	0.003	0.0028
	q_e ($mg{\cdot}g^{-1}$)	36.2	22.3	38.6
	R^2	0.951	0.78	0.900
Pseudo–second–order	K_2 ($g{\cdot}mg^{-1}{\cdot}min^{-1}$)	0.00065	0.001	0.00060
	q_e ($mg{\cdot}g^{-1}$)	101.8	126.3	359.7
	R^2	0.995	0.996	0.998
Intraparticle diffusion	K_{1d} ($mg{\cdot}g^{-1}{\cdot}min^{-1/2}$)	15.96	4.35	17.09
	C_1	6.43	94.02	271.68
	R_1^2	0.933	0.84	0.911
	K_{2d} ($mg{\cdot}g^{-1}{\cdot}min^{-1/2}$)	2.56	0.49	1.210
	C_2	59.43	110.66	326.3
	R_2^2	0.729	0.91	0.517
	K_{3d} ($mg{\cdot}g^{-1}{\cdot}min^{-1/2}$)	0.64	0.47	0.70
	C_3	79.37	109.41	333.82
	R_3^2	0.923	0.9	0.966

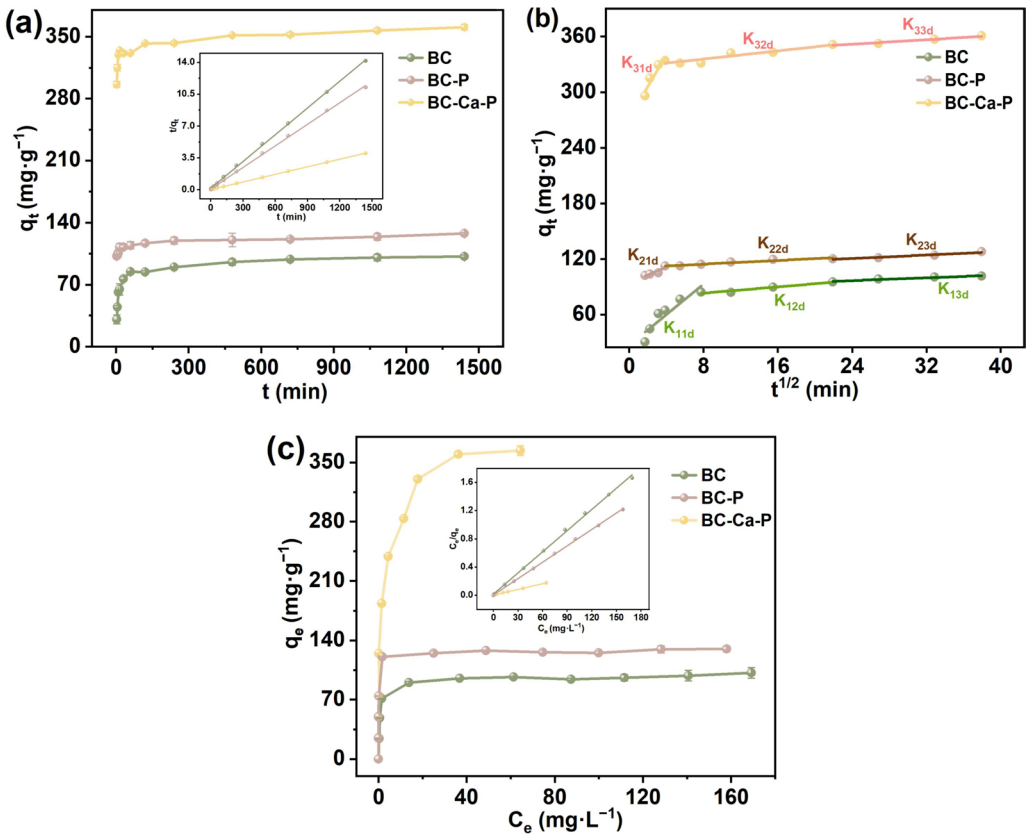

Fig. 3 Pb(II) adsorption model by BC, BC-P, and BC-Ca-P. **a** Effect of contact time on Pb(II) adsorption (inset: pseudo–second–order kinetic model plots); **b** intraparticle diffusion kinetic model plots; **c** isotherm plots for Pb(II) adsorption (inset: Langmuir isotherm model plots)

to the peak at 2925 cm^{-1} (Luo et al. 2021). All the adsorbents possessed the basic functional groups of biochar. After loading Ca onto BC, the CO_3^{2-} stretching peak at 1387 cm^{-1} was enhanced (Wang et al. 2021). Notably, at 571 cm^{-1}, an O-P-O bending peak was seen, indicating that P was present in trace levels in BC and BC-P. Following P adsorption by BC-Ca, there was a considerable enhancement of the peaks at 1030, 975, and 543–573 cm^{-1}, which related to P-O stretching, O-P-C, and O-P-O bending vibrations, respectively. This suggests that BC-Ca absorbed a greater amount of P.

3.2 Batch adsorption process comparison

3.2.1 Influence of initial pH

As indicated in Fig. 2, the pH_{PZC} values of the BC, BC-P, and BC-Ca-P adsorbents were 3.26, 2.50, and 3.29, respectively. The Pb(II) adsorption capabilities of BC, BC-P, and BC-Ca-P were the lowest at an initial pH of approximately 2, and reached their maximum at pH 5. This occurred because when the solution pH dropped below pH_{PZC}, the surface of the adsorbents was positively charged due to protonation, Pb(II) was repelled, and the H^+ in the solution competed with Pb(II) owing to a limited number of adsorption sites. Meanwhile, Ca in BC-Ca-P is dissolved, resulting in the reduction of its P content, and the adsorption performance of Pb(II) was poor. When the solution pH surpassed that of pH_{PZC}, the surface of the adsorbent was deprotonated and had a negative charge and surface electrostatic attraction occurred, improving Pb(II) adsorption (Deng et al. 2018).

3.2.2 Modeling of adsorption kinetics

Adsorption kinetics were examined using a variety of kinetic models, including the intraparticle diffusion equation, pseudo–first–order, and pseudo–second–order models, following Eqs. (1), (2) and (3), respectively (Li et al. 2022a).

$$ln(q_e - q_t) = lnq_e - K_1 t. \quad (1)$$

$$\frac{t}{q_t} = \frac{1}{K_2 {q_e}^2} + \frac{1}{q_e} t. \quad (2)$$

$$q_t = K_{jid} t^{1/2} + C_i. \quad (3)$$

where q_t ($mg \cdot g^{-1}$) is the amount of adsorbed substance at time t, q_e ($mg \cdot g^{-1}$) is the amount of adsorbed substance at equilibrium, K_1 (min^{-1}) is the pseudo–first–order rate constant, K_2 ($g \cdot mg^{-1} \cdot min^{-1}$) is the pseudo–second–order rate constant, K_{jid} ($mg \cdot g^{-1} \cdot min^{-1/2}$) represents the diffusion rate constant within stage i (j represents a certain adsorbent, BC: j = 1, BC-P: j = 2, BC-Ca-P: j = 3) and C_i is related to the thickness of the boundary layer during the diffusion process.

Figure 3a shows that the adsorption of Pb(II) by BC, BC-P, and BC-Ca-P reached equilibrium in a relatively short time. In the first 5 min, Pb(II) was rapidly adsorbed, followed by a slower rate as the quantity of surface adsorption sites decreased until equilibrium was reached over 2 h, indicating that the adsorbents could rapidly capture Pb(II). As shown in Table 1, the pseudo–second–order model's R^2 values exceeded 0.99, making it larger than the pseudo–first–order model. The equilibrium adsorption capabilities of BC, BC-P, and BC-Ca-P were also determined to be 101.83, 126.26, and 359.71 $mg \cdot g^{-1}$, respectively, and these values were closer to the corresponding experimental maximum adsorption capabilities (101.6, 127.9, and 360.7 $mg \cdot g^{-1}$). Therefore, the adsorption of Pb(II) onto the adsorbents was better represented by the pseudo–second–order model. It is speculated that the Pb(II) concentration and quantity of active sites can have an impact on the adsorption process, and the adsorption rate may be dominated by chemisorption (Wadhawan et al. 2020).

To fully describe the diffusion mechanisms throughout the adsorption processes of BC, BC-P, and BC-Ca-P, an intraparticle diffusion model was fitted to analyze the adsorption of Pb(II). The adsorption process consisted of three steps: external diffusion, internal diffusion, and adsorption (Fig. 3b). Since the straight line did not pass through the origin, there were other rate-controlling steps besides intraparticle diffusion (Luo et al. 2021). First stage Pb(II) adsorption rate constants for BC, BC-P, and BC-Ca-P were higher than second and third stage values ($K_{1d} > K_{2d} > K_{3d}$), indicating that diffusion occurred more rapidly during the first stage. This was primarily because the adsorption rate was controlled by the mass-transfer rate of Pb(II) from the adsorbent's outer to inner

Table 2 Langmuir, Freundlich, and Temkin isotherm model parameters of BC, BC-P, and BC-Ca-P

Models	Parameters	Adsorbents		
		BC	BC-P	BC-Ca-P
Langmuir	q_{max} ($mg \cdot g^{-1}$)	99.1	128.7	361.2
	K_L ($L \cdot mg^{-1}$)	0.56	1.66	0.88
	R^2	0.998	0.997	0.997
Freundlich	K_F ($mg \cdot g^{-1} \cdot L^{1/n} \cdot mg^{-1/n}$)	46.8	68.5	150.0
	1/n	0.17	0.15	0.26
	R^2	0.762	0.71	0.957
Temkin	K_T ($L \cdot mg^{-1}$)	171.9	1331.6	257.4
	F ($J \cdot mol^{-1}$)	10.21	11.23	36.44
	R^2	0.875	0.83	0.959

surface (Deng et al. 2021). There were a lot of adsorption sites on the surface during the first stage, but as adsorption advanced, the number of sites shrank. In addition, the C values reflected the effect of the boundary layer of the liquid phase on the adsorption rate. The results ($C_3 > C_2 > C_1$) indicated that the thickness of the boundary layer in the third stage had the greatest influence on the adsorption rate. In addition, the adsorption rate constant of BC-Ca-P in the first stage (K_{1d}) was higher than those of BC and BC-P, because there were more adsorption sites for Pb(II) on the surface of BC-Ca-P, based on the effective collision theory.

3.2.3 Modeling of adsorption isotherms

The experimental data were fitted using the Langmuir, Freundlich, and Temkin models using Eqs. (4), (5), and (6), respectively (Qiu et al. 2022b).

$$\frac{C_e}{q_e} = \frac{C_e}{q_{max}} + \frac{1}{K_L q_{max}}. \tag{4}$$

$$lnq_e = \frac{1}{n} lnC_e + lnK_F. \tag{5}$$

$$q_e = F(\ln K_T + \ln C_e). \tag{6}$$

where K_L ($L \cdot mg^{-1}$) is the Langmuir adsorption equilibrium constant; K_F ($mg \cdot g^{-1} \cdot L^{1/n} \cdot mg^{-1/n}$) and n are the Freundlich adsorption capacity and adsorption constant, respectively; q_e ($mg \cdot g^{-1}$) is the equilibrium adsorption capacity; q_{max} ($mg \cdot g^{-1}$) is the maximum adsorption capacity; C_e ($mg \cdot L^{-1}$) is the equilibrium concentration of pollutants; K_T ($L \cdot mg^{-1}$) is the constant related to the equilibrium binding energy; and F ($J \cdot mol^{-1}$) is the constant related to the heat of adsorption.

As seen in Fig. 3c, the equilibrium adsorption quantities of BC, BC-P, and BC-Ca-P rose with an increase in the starting concentration of Pb(II) at pH 5. BC-Ca-P had a larger equilibrium adsorption capability than BC and BC-P. In Table 2, the higher correlation coefficients for the Langmuir fits indicated that the Freundlich and Temkin equations may not sufficiently describe the experimental data; instead, the Langmuir equation may. This revealed that Pb(II) was eliminated by monolayer adsorption on the surfaces of BC, BC-P, and BC-Ca-P across a uniform distribution of active sites (Liu et al. 2021; Shao et al. 2023). The maximum Pb(II) adsorption capacities of BC, BC-P, and BC-Ca-P were determined by the Langmuir model calculations to be 99.10, 128.70, and 361.20 $mg \cdot g^{-1}$, respectively. These values were in closer agreement with the respective experimental maximum adsorption capacity (101.8, 130.0, and 363.8 $mg \cdot g^{-1}$). Therefore, BC-Ca-P exhibited better adsorption performance than BC and BC-P.

Online Resource Table S2 summarizes the maximum Pb(II) adsorption capacity of different kinds of phosphorus-modified biochar adsorbents. Under the same experimental conditions, the adsorption capacity of

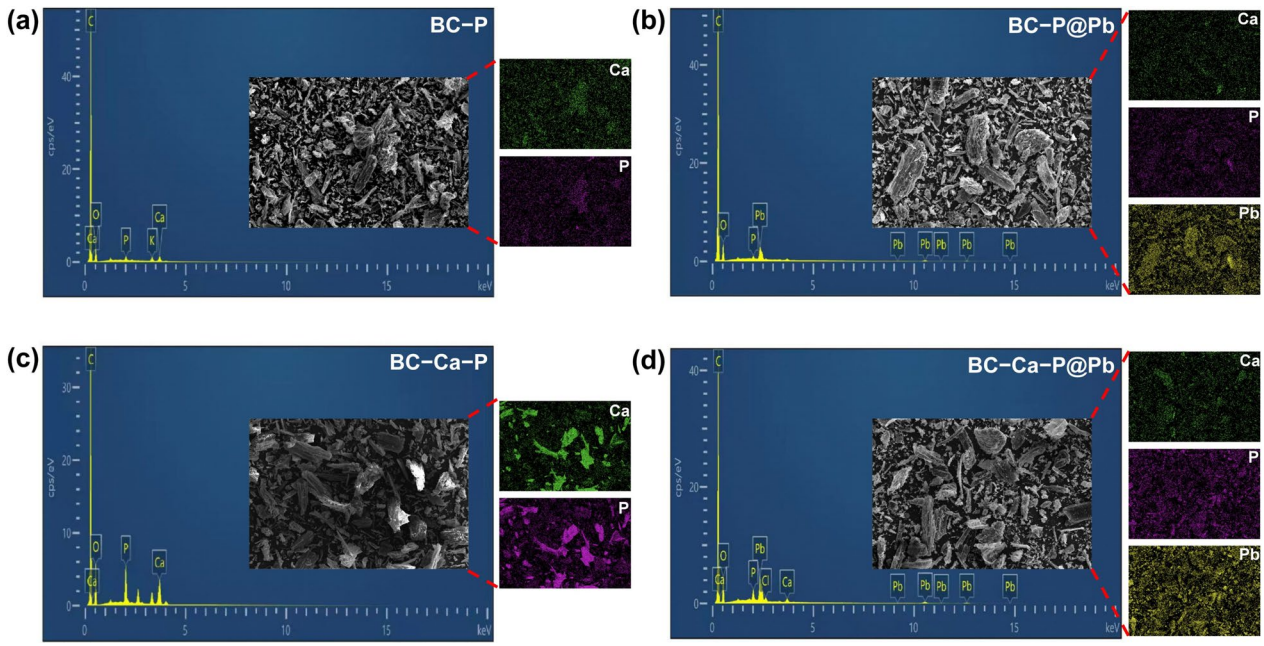

Fig. 4 SEM images and EDS results (Ca, P, and Pb) of **a** BC-P, **b** BC-P@Pb, **c** BC-Ca-P, and **d** BC-Ca-P@Pb. Note: BC-P after Pb(II) adsorption (BC-P@Pb) and BC-Ca-P after Pb(II) adsorption (BC-Ca-P@Pb)

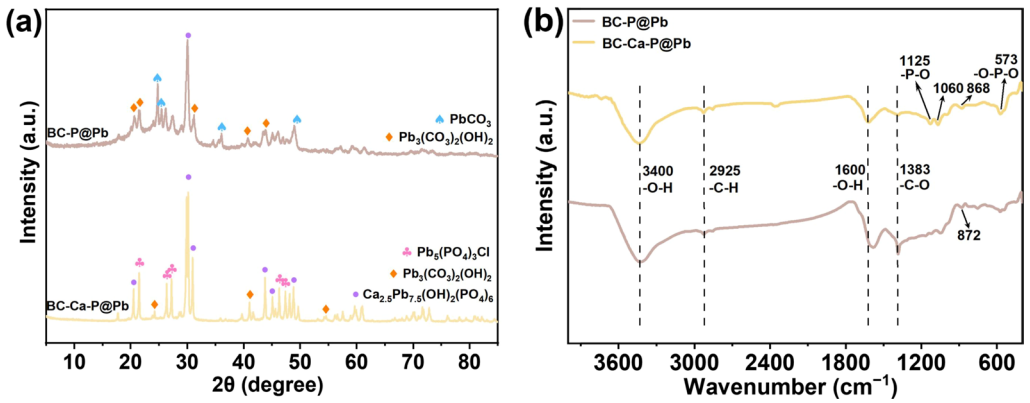

Fig. 5 **a** XRD patterns. **b** FTIR spectra of BC-P, BC-P@Pb, BC-Ca-P, and BC-Ca-P@Pb. Note: BC-P after Pb(II) adsorption (BC-P@Pb) and BC-Ca-P after Pb(II) adsorption (BC-Ca-P@Pb)

P-modified biochar for Pb(II) was much higher than that of virgin biochar. This phenomenon indicated that the increase in biochar phosphorus content played a crucial role in improving its adsorption performance for Pb(II). However, the above studies used exogenous phosphates to modify biochar. This external addition of P not only increased costs, but potentially caused secondary pollution to the environment. Notably, unlike the traditional P-modified adsorbents, the BC-Ca-P used in this study was the waste of dephosphorized adsorbent, which did not require the addition of external P, and can realize the resource recovery and utilization of waste. In our study, the removal efficiency of Pb(II) by BC-Ca-P was significantly better than that of BC-P, because the adsorption capacity of phosphorus by BC-Ca (64.05 $mg{\cdot}g^{-1}$) was much higher than that of BC (3.85 $mg{\cdot}g^{-1}$). As a result, the adsorption capacity of Pb(II) by BC-Ca-P was 2.8 times higher than that of BC-P. This phenomenon also confirmed that higher phosphorus content can improve the adsorption performance of Pb(II), which is consistent with previous research conclusions. Compared to other studies, BC-Ca-P had a greater Pb(II) adsorption capacity (about 4.6 times that of H_3PO_4-modified chicken feather biochar), whereas the equilibrium time of BC-Ca-P was much shorter than that of the other phosphorous-modified adsorbents (sharp decrease from 25 to 2 h). Dephosphorization waste BC-Ca-P exhibited excellent heavy metal absorption performance, demonstrating the feasibility of "using waste to treat waste".

3.2.4 Selective adsorption study

BC-Ca-P had good, but varying, adsorption capacity for the prevention and control of the "national priority" heavy metals (Pb(II) > Cd(II) > Zn(II) > Cu(II) > Ni(II) > Mn(II)) under the same reaction conditions (Online Resource Fig. S2). The reason behind this could be the significant variations in the binding affinities between activated sites and heavy metal ions. Large differences exist in the ionic characteristics (e.g., ion surface charge density, radius, and charge number) of different heavy metal ions. Specifically, the hydration energy decreases with an increase in atomic coefficient and ionic radius, and the hydration radius decreases for heavy metal ions with the same charge. The surface effective positive charge density of heavy metal ions is large, and the functional groups that are negatively charged on the surface provide active sites with a greater binding affinity for heavy metal ions (Du et al. 2016). As Pb(II) possesses a relatively larger surface effective positive charge density than other metal ions, it binds more strongly to activated sites.

3.3 Mechanism study

3.3.1 Characterization analysis

We contradistinguished and analyzed the mechanism of Pb(II) removal by dephosphorization waste (BC-Ca-P) and exogenous P-modified biochar (BC-P). The SEM–EDS results (Fig. 4) demonstrate that the surface morphology of the raw materials and materials following lead adsorption did not change significantly. Lead was detected (5.87% for BC-P@Pb and 8.96% for BC-Ca-P@Pb) after, but not before, adsorption, indicating that BC-P and BC-Ca-P were successful in adsorbing Pb(II). BC-Ca-P@Pb exhibited a higher Pb percentage than BC-P@Pb and BC@Pb, indicating that BC-Ca-P had better performance to eliminate Pb(II). The Pb(II) content of the materials increased with increasing P content. Additionally, the surface distribution of Pb(II) was essentially the same as that of P based on the EDS spectra, indicating that P provided adsorption sites for Pb(II).

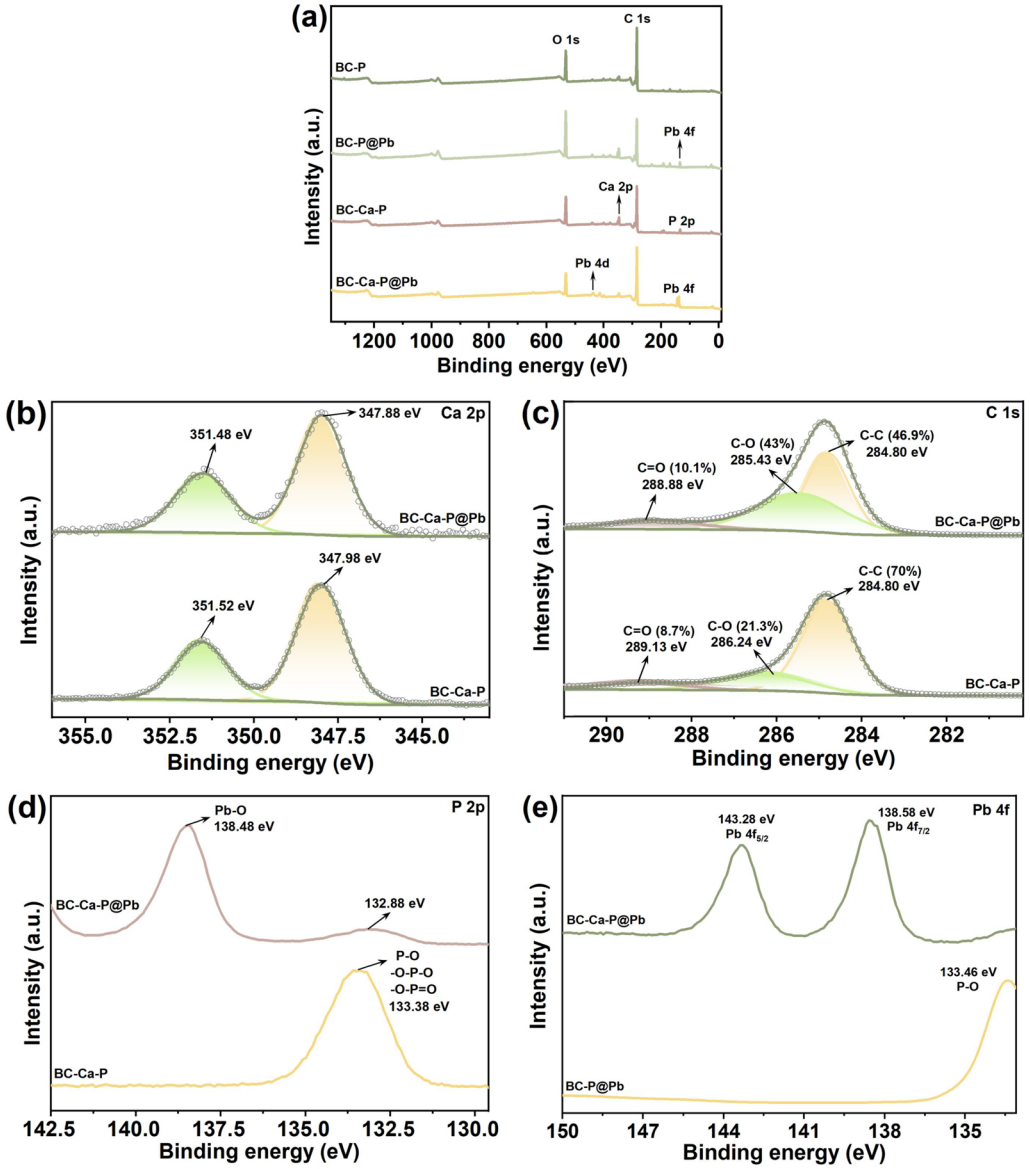

Fig. 6 **a** XPS full spectra of BC-P, BC-P@Pb, BC-Ca-P, and BC-Ca-P@Pb; **b** Ca 2p; **c** C1s; **d** P 2p; and **e** Pb 4f peak spectra of BC-Ca-P and BC-Ca-P@Pb. Note: BC-P after Pb(II) adsorption (BC-P@Pb) and BC-Ca-P after Pb(II) adsorption (BC-Ca-P@Pb)

The deep mechanism was explored using XRD, FTIR, and XPS. The XRD results (Fig. 5a) illustrated that the $CaCO_3$ peak disappeared, whereas $Pb(CO_3)_2(OH)_2$ and $PbCO_3$ (PDF#98–000–0153) diffraction peaks appeared following Pb(II) adsorption by BC-P. The $CaHPO_4$ and $CaHPO_4(H_2O)_2$ peaks disappeared, whereas $Pb(CO_3)_2(OH)_2$, $Ca_{2.5}Pb_{7.5}(OH)_2(PO_4)_6$, and $Pb_5(PO_4)_3Cl$ peaks appeared after the adsorption of Pb(II) by BC-Ca-P. These results indicated that BC-P and BC-Ca-P reacted with Pb(II) by chemical precipitation (Xu et al. 2021a).

The FTIR results (Fig. 5b) showed that the –C–O functional group intensity at 1383 cm^{-1} was diminished following Pb(II) adsorption by BC-P and BC-Ca-P. The intensities of the functional groups containing P in BC-P and BC-Ca-P weakened and were displaced. These results proved that abundant functional groups, including –OH, P-O, P=O C-O, and C=O, were involved in complexation or chemical precipitation with Pb(II) (Qu et al. 2023a). Besides, the peak intensities of more functional groups in BC-Ca-P changed, indicating excellent adsorption performance toward Pb(II).

The chemical composition changes of materials before and after adsorption of Pb(II) were compared by XPS characterization (Fig. 6). Before adsorption, BC-Ca-P

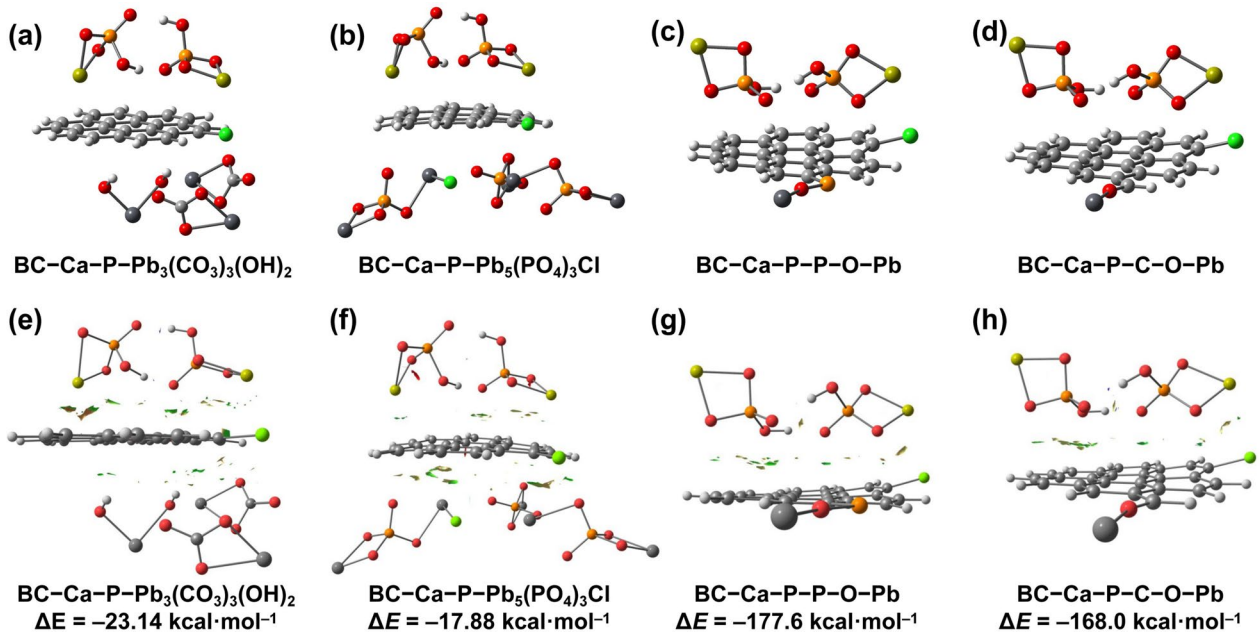

Fig. 7 Interaction energies of material structures containing different functional groups for Pb(II) adsorption (**a**–**d**) and NCI (**e**–**h**). Note: noncovalent interactions (NCI)

primarily exhibited characteristic peaks of C 1 s, O 1 s, Ca 2p, and P 2p (Fig. 6a). BC-P primarily exhibited prominent characteristic peaks of C 1 s and O 1 s, with a weak peak of P 2p due to the lower P uptake of pristine biochar (Fig. 6a). After the adsorption of Pb(II), the P 2p peaks of BC-Ca-P and BC-P disappeared. New Pb 4f and Pb 4d peaks in BC-Ca-P@Pb appeared, whereas only the Pb 4f peak in BC-P@Pb was detected (Fig. 6a). This supported the SEM–EDS analysis by showing that P was involved in Pb(II) adsorption by BC-Ca-P and BC-P (Lian et al. 2020). Further, the small change in the Ca 2p binding energy of BC-Ca-P (Fig. 6b) indicated that a small amount of Ca participated in the adsorption reaction. In contrast, there were notable changes in the binding energies of P-O and P=O and C-O and C=O (Fig. 6c and d). Two parts were identified from the high–definition Pb 4f XPS spectrum: Pb 4f7/2 and Pb 4f5/2 (Fig. 6e), demonstrating that Pb(II) had a chemical reaction with the surface functional groups of the biochar (Liu et al. 2023c). Combined with the FTIR and XRD results, these functional groups on BC-Ca-P were the main adsorption sites.

Moreover, BC-Ca-P and BC-P could remove Pb(II) through pore filling based on the BET analysis, demonstrating their porous structure. Combined with zeta

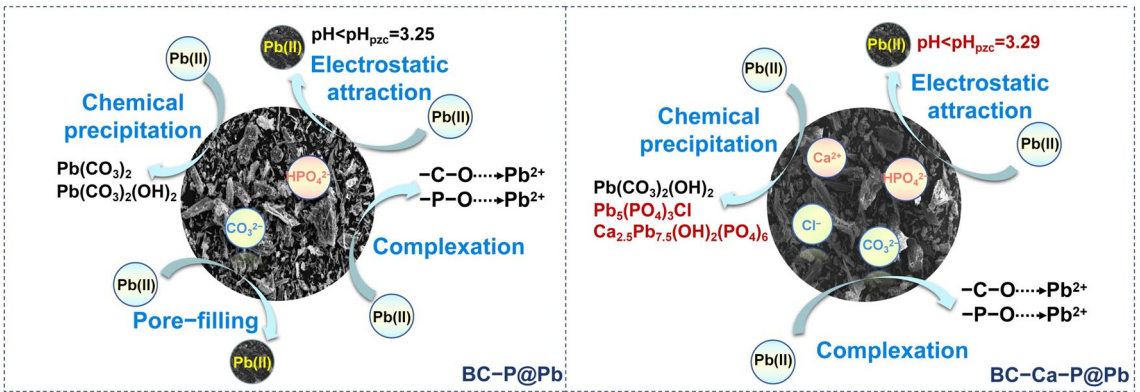

Fig. 8 The main pathways and differences of Pb(II) adsorption between BC-P and BC-Ca-P

potential analysis, electrostatic attraction also promoted the adsorption process.

3.4 DFT calculation

Based on a prior study, the surface model of the aromatized pristine biochar was imitated by a seven-ring pure graphene structure (Sun et al. 2023). It is clear from the results that several types of binding forms existed between BC-Ca-P and Pb(II), including BC-Ca-P-$Pb_3(CO_3)_3(OH)_2$, BC-Ca-P-$Pb_5(PO_4)_3Cl$, BC-Ca-P-P-O-Pb, and BC-Ca-P-C-O-Pb, during the adsorption processes. DFT calculations were performed to further verify and analyze the adsorption binding forms. The optimized geometries of BC-Ca-P, $Pb_3(CO_3)_3(OH)_2$, $Pb_5(PO_4)_3Cl$, BC-Ca-P-P-O, and BC-Ca-P-C-O are shown in Online Resource Fig. S3. Figure 7 displays the interaction energies of carbon structures with diverse functional groups on Pb(II).

The interaction energies for BC-Ca-P-$Pb_3(CO_3)_3(OH)_2$, BC-Ca-P-$Pb_5(PO_4)_3Cl$, BC-Ca-P-P-O-Pb, and BC-Ca-P-C-O-Pb complexes were −23.14, −17.88, −177.6, and −168.0 kcal·mol^{-1}, respectively. The results indicated that BC-Ca-P-P-O and BC-Ca-P-C-O strongly adsorbed Pb(II), in which BC-Ca-P-P-O and BC-Ca-P-C-O coordinated with Pb(II), whereas BC-Ca-P adsorbed $Pb_3(CO_3)_3(OH)_2$ or $Pb_5(PO_4)_3Cl$ through weak intermolecular interactions, as revealed by NCI analyses in which green clouds appeared between BC-Ca-P and $Pb_3(CO_3)_3(OH)_2$ (or $Pb_5(PO_4)_3Cl$).

The molecular electrostatic potential (MESP) can be employed to illustrate the accepting and donating of electrons (Sun et al. 2023). The MESP maps for BC-Ca-P and its different binding forms with Pb(II) are shown in Online Resource Fig. S4. The MESPs on BC-Ca-P, BC-Ca-P-$Pb_3(CO_3)_3(OH)_2$, and BC-Ca-P-$Pb_5(PO_4)_3Cl$ indicated that the rich electrons on BC-Ca-P enabled it to adsorb $Pb_3(CO_3)_3(OH)_2$ and $Pb_5(PO_4)_3Cl$ to form stable complexes, whereas the MESPs on BC-Ca-P-P-O-Pb and BC-Ca-P-C-O-Pb suggested that BC-Ca-P-P-O and BC-Ca-P-C-O acted as good electron donors to coordinate with Pb(II).

According to the molecular orbital calculations (Online Resource Fig. S5), the E_{gap} values of BC-Ca-P containing different functional groups were lower than those of the pure graphene structure (4.05 eV) (Sun et al. 2023), indicating a higher likelihood of electron

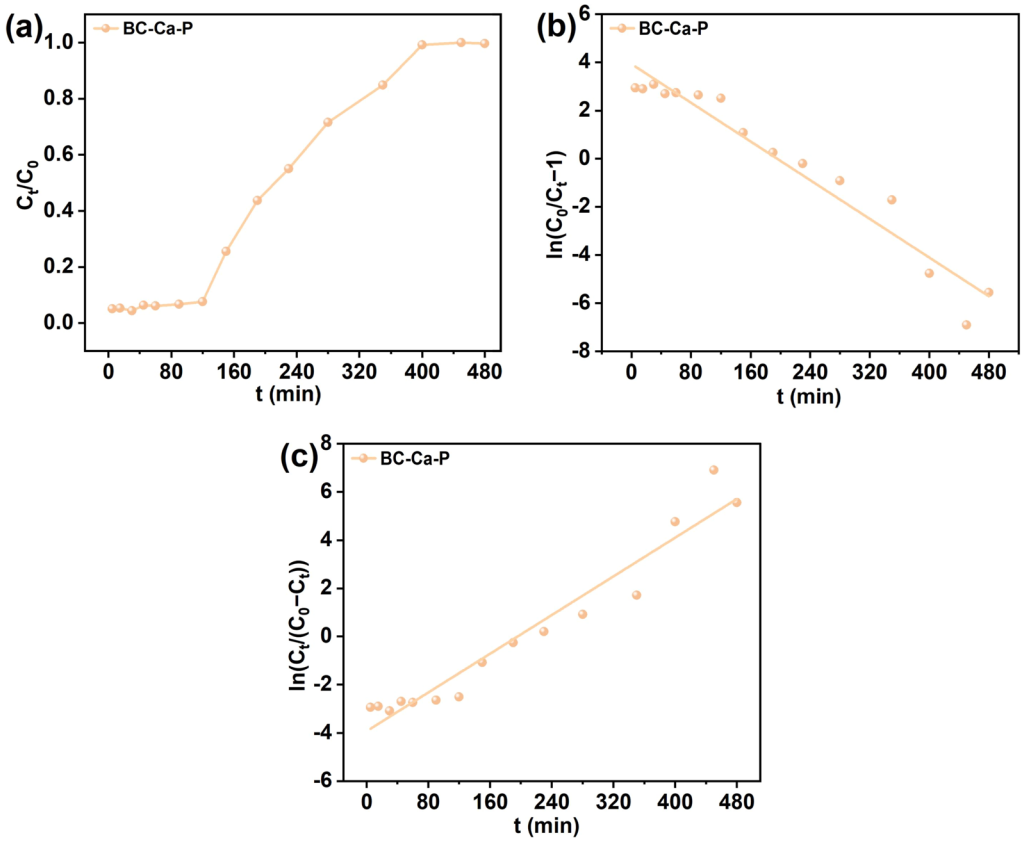

Fig. 9 **a** Breakthrough curves of the continuous-flow adsorption process of BC-Ca-P; **b** Thomas model plots;**c** Yoon–Nelson model plots for the continuous-flow adsorption process of BC-Ca-P

transfer and cluster molecules stability after BC modification. This is due to the addition of functional groups containing Ca and P increasing the amount of electrons available to boost chemical activity and quickening the pace of electron transfer. These results further confirmed that BC-Ca-P had better adsorption performance than BC toward Pb(II).

The main pathways and differences of Pb(II) adsorption between BC-P and BC-Ca-P are shown in Fig. 8.

3.5 Practical application process investigation

3.5.1 Pb(II) adsorption by actual dephosphorization waste

Online Resource Fig. S6 shows the feasibility of Pb(II) removal using dephosphorization waste (BC-Ca-P) recovered from a practical application scenario. Phosphorus uptake by BC-Ca (64.05 $mg{\cdot}g^{-1}$) was greater than that by BC (3.85 $mg{\cdot}g^{-1}$) because of the strong binding between Ca and P, consistent with the P percentage comparison results of the former characterization. When BC-P and BC-Ca-P were applied with the same dosage, BC-Ca-P showed better field Pb(II) adsorption performance (389.7 $mg{\cdot}g^{-1}$, approximately four times more than the BC-P value) owing to the greater accumulation of P, similar to the results of laboratory-scale comparisons of BC-P and BC-Ca-P. This result once again confirmed that the increase in phosphorus content of biochar played a crucial role in improving its adsorption performance for Pb (II). Therefore, this study primarily focused on BC-Ca-P.

Notably, in the field, BC-Ca-P showed a slightly higher adsorbed amount of Pb(II) than that revealed by laboratory results. This may be because it contained more water-soluble organic substances during actual wastewater treatment, improving adsorption capacity via complexation. These results show that using dephosphorization waste (BC-Ca-P) obtained from the field for efficient heavy metal (Pb) removal is both feasible and promising.

3.5.2 Continuous-flow adsorption process

Figure 9 shows the dynamic adsorption of Pb(II) onto BC-Ca-P. The time point at which $C_t/C_0 = 0.1$, corresponding to the breakthrough time (t_b), was taken as the adsorption breakthrough point. The exhaust time (t_e) corresponded to the time point when $C_t/C_0 = 0.9$, indicating that the adsorption of BC-Ca-P had achieved saturation. The breakthrough and exhaust times were approximately 130 and 360 min, respectively. The total quantity of Pb(II) adsorbed during the entire process was computed from the integration area of time under a certain flow rate and initial concentration using Eq. (7). The dynamic adsorption capacity of BC-Ca-P was calculated using Eq. (8).

$$q_t = \frac{QA}{1000} = \frac{Q}{1000}\int_{t=0}^{t=t_e}(C_0 - C_t)dt \tag{7}$$

$$q_e = \frac{q_t}{m} \tag{8}$$

where C_0 ($mg{\cdot}L^{-1}$) and C_t ($mg{\cdot}L^{-1}$) are the influent and effluent Pb(II) concentrations, m (g) is the column adsorbent mass, Q ($mL{\cdot}min^{-1}$) is the influent flow rate, q_t ($mg{\cdot}g^{-1}$) is the total adsorption capacity of Pb(II), q_e ($mg{\cdot}g^{-1}$) is the average adsorption capacity of Pb(II), and A is the area of the penetration curve (cm^2).

In light of the previously mentioned equations, the dynamic adsorption capacity of BC-Ca-P (312.79 $mg{\cdot}g^{-1}$) was lower than the equilibrium static adsorption uptake (361.20 $mg{\cdot}g^{-1}$). This was primarily because of the continuous-flow treatment during the dynamic adsorption process having a shorter solid-liquid contact time than the intermittent-flow treatment used in batch experiments (Du et al. 2018). As industrial wastewater is often treated in a continuous-flow manner, the results obtained regarding the dynamic adsorption capacity could better predict Pb(II) removal in practical industrial wastewater treatment (Yang et al. 2022).

To gain a deeper understanding of fixed-bed adsorption, the Thomas and Yoon–Nelson models were applied to estimate dynamic adsorption parameters, using Eqs. (9) and (10) for linear fitting (Du et al. 2018):

$$ln\left(\frac{C_0}{C_t} - 1\right) = \frac{K_{TH}q_0 m}{Q} - K_{TH}C_0 \tag{9}$$

$$ln\left(\frac{C_t}{C_0 - C_t}\right) = K_{YN}t - K_{YN}\tau \tag{10}$$

where K_{Th} ($mL{\cdot}min^{-1}{\cdot}mg^{-1}$) is the Thomas rate constant, K_{YN} (min^{-1}) is the Yoon–Nelson rate constant, τ (min) is the time required for 50% breakthrough, and q_0 ($mg{\cdot}g^{-1}$) is the solid loading per unit mass of adsorbent.

Online Resource Table S3 shows Yoon–Nelson and Thomas models gave an excellent match to the experimental data ($R^2 > 0.9$). The Thomas model prediction of the dynamic adsorption capacity was 312.8 $mg{\cdot}g^{-1}$, in proximity to the experimental data (312.79 $mg{\cdot}g^{-1}$). The Thomas model assumes no axial diffusion when the solution flows across the column, whereas the pseudo–second–order kinetic model describes the adsorption process and estimates the dynamic adsorption capability. The results illustrated that the adsorption of Pb(II) followed a pseudo–second–order kinetic reaction. Thus, the Thomas model accurately described the continuous-flow adsorption process. The Yoon–Nelson model calculated that BC-Ca-P had a 50% breakthrough time of

195.49 min, close to the experimental value (190 min), accurately predicting the 50% breakthrough time. There were some deviations between the model predictions and experimental values. This might have happened as a result of the model oversimplifying the actual circumstances and ignoring the geometric characterization of the column or the adsorbents' physicochemical and structural characteristics.

3.5.3 P leaching test

The risk of secondary pollution from P leaching from dephosphorization waste during heavy metal treatment was assessed. As illustrated in Fig. S7 (Online Resource), P leaching was observed in BC-Ca-P during heavy metal treatment. Generally, the P leaching concentration in the water was higher than that in the $Pb(NO_3)_2$ solution. This may have been because the chemical adsorption between P and Pb(II) could help fix more P on the biochar's surface and reduce P loss. The amount of P leached from BC-Ca-P increased over time, reaching an equilibrium within approximately 960 min. The highest P leaching concentration was well below the phosphate discharge level I standard (0.5 mg $P{\cdot}L^{-1}$) of the Chinese "Comprehensive Sewage Discharge Standard."

The dynamic Pb(II) adsorption capability of BC-Ca-P was 312.8 $mg{\cdot}g^{-1}$ (300 $mg{\cdot}g^{-1}$ for easy calculation) with an exhaustible time of 130 min, which was treated as the adsorbent replacement period. The P leaching amount per unit mass of BC-Ca-P in one field adsorbent replacement period was approximately 0.02 mg $P{\cdot}g^{-1}$ (Online Resource Fig. S7). Scaling the experimental data, a ton of dephosphorization waste (BC-Ca-P) could be used for the remediation of three million liters of lead-polluted water (initial Pb(II) concentration of 100 $mg{\cdot}L^{-1}$). The P leaching concentration was 0.0067 mg $P{\cdot}L^{-1}$ (see Online Resource for calculation details), well below the standard value (0.5 mg $P{\cdot}L^{-1}$) under this circumstance. Thus, the P leakage risk during heavy metal removal by dephosphorization waste is negligible.

4 Conclusions and environmental implications

In this study, Ca-modified biochar was prepared from tobacco stalks and $CaCl_2$ (an inexpensive chemical agent). BC-Ca-P was recovered after Ca-modified biochar was used for efficient treatment of P-containing wastewater, and successfully utilized to remove heavy metals, providing a sustainable method to utilize dephosphorization waste for heavy metal removal. Based on Langmuir fitting, the maximum adsorption capability of BC-Ca-P for Pb(II) was 361.20 $mg{\cdot}g^{-1}$ at pH 5.0. Adsorption reached an equilibrium state after 2 h, fitting pseudo–second–order kinetics well ($R^2 = 0.998$). BC-Ca-P had good adsorption capacity for different heavy metal ions (Pb(II) > Cd(II) > Zn(II) > Cu(II) > Ni(II) > Mn(II)). BC-Ca-P recovered from actual P-containing wastewater showed better Pb(II) adsorption performance (389.7 $mg{\cdot}g^{-1}$, approximately four times greater than that of BC-P). Thomas and Yoon–Nelson models accurately described the breakthrough curves of the continuous-flow adsorption process ($R^2 > 0.90$) and predicted that the saturated adsorption capacity was 312.8 $mg{\cdot}g^{-1}$ and 50% breakthrough time was 195.49 min. The phosphate leaching test results demonstrated that P leaching was only 0.02 mg $P{\cdot}L^{-1}$, which was well below the value set by the Chinese national standard (0.5 mg $P{\cdot}L^{-1}$), indicating a negligible P leakage risk during heavy metal treatment.

According to the XRD, FTIR, and XPS characterization, the exceptional adsorption performance of BC-Ca-P for Pb(II) was primarily due to the presence of abundant oxygen-containing functional groups on the surface of the biochar, which could promote complexation or chemical precipitation with Pb(II). Besides, physical adsorption via mechanisms such as pore filling, electrostatic attraction, and hydrogen bonding also played a facilitating role. According to the DFT calculation results, the oxygen-containing functional groups (P-O and C-O) introduced into the biochar structure had higher adsorption energies, indicating an important role during Pb(II) uptake by BC-Ca-P. The introduction of Ca/P atoms into biochar provided more electrons to enhance chemical activity and accelerate the electron transfer rate, leading to higher adsorption of Pb(II).

In traditional low-carbon footprint disposal, the combustion of dephosphorization waste tends to increase greenhouse gas emissions, while the operation cost of solid waste landfill is high. In contrast, it is feasible, meaningful, and promising to use dephosphorization waste for heavy metal removal. This is an eco–friendly waste-reduction and resource-utilization method. Unlike traditional P-modified biochar, the recovery of dephosphorization waste does not require the addition of external P, which not only saves material acquisition costs, but also realizes the resource utilization of P, and even can alleviate secondary pollution of P. It has multiple benefits and broad application prospects. In summary, the recycling and reuse of dephosphorization waste in this study is of great significance for water pollution control, resource utilization, and environmental protection. Our study, though successful, was principally conducted in a laboratory. Future work should focus on studies to enhance the adsorption ability and process optimization for the field application of BC-Ca-P. Furthermore, the addition of BC-Ca-P to soil has the dual effect of heavy metal remediation and fertility improvement, which is beneficial for the safety of the soil environment and

meets the phosphorus demand of crops. Therefore, we need to further explore relevant fields to promote the health and sustainable use of soil.

Supplementary Information

The online version contains supplementary material available at https://doi.org/10.1007/s42773-024-00373-8.

Additional file 1.

Acknowledgements
The corresponding author would like to acknowledge the National Natural Science Foundation of China (42107081) and the Fundamental Research Funds for the Central Public Research Institutes (2023—jbkyywf—dzl).

Author contributions
All authors contributed to this study's conception and design. Investigation, visualization, methodology, software, data curation, formal analysis, and writing–original draft were performed by Weilin Fu and Mengmeng Li, who contributed equally to this work. Methodology, visualization, and formal analysis were performed by Hongan Chen. Methodology and software analysis were performed by Jianhua Qu. Methodology and resources were performed by Lisheng Zhang. Methodology and validation were performed by Shangkai Qiu. Validation was performed by Menghan Feng. Formal analysis was performed by Mingyao Yuan. Software analysis was performed by Changbin Guo. Methodology was designed by Jien Zhou. Writing–original draft, writing–review and editing, project administration, conceptualization, and supervision were performed by Zhaolin Du. Writing–review and editing, validation, and supervision were performed by Feng Wang. All authors read and approved the final manuscript.

Funding
This research was financially supported by the National Natural Science Foundation of China (42107081) and the Fundamental Research Funds for the Central Public Research Institutes (2023–jbkyywf–dzl).

Availability of data and materials
The datasets used or analyzed during the current study are available from the corresponding author on reasonable request.

Declarations

Competing interests
The authors declare that they have no known competing financial interests or personal relationships that could have appeared to influence the work reported in this paper.

Author details
[1]Ministry of Agriculture and Rural Affairs, Agro—Environmental Protection Institute, Tianjin 300191, China. [2]Dali Comprehensive Experimental Station of Environmental Protection Research and Monitoring Institute, Ministry of Agriculture and Rural Affairs (Dali Original Seed Farm), Dali 671004, China. [3]Ministry of Agriculture and Rural Affairs, Xiangtan Experimental Station of Agro—Environmental Protection Institute, Xiangtan 411199, Hunan, China. [4]School of Resources and Environment, Northeast Agricultural University, Harbin 150030, China.

Received: 15 March 2024 Revised: 3 August 2024 Accepted: 11 August 2024
Published online: 11 September 2024

References

Almanassra IW, Mckay G, Kochkodan V, Ali Atieh M (2021) A state of the art review on phosphate removal from water by biochars. Chem Eng J 409:128211. https://doi.org/10.1016/j.cej.2020.128211

Cao H, Wu X, Syed-Hassan SSA, Zhang S, Mood SH, Milan YJ, Garcia—Perez M, (2020) Characteristics and mechanisms of phosphorous adsorption by rape straw—derived biochar functionalized with calcium from eggshell. Bioresour Technol 318:124063. https://doi.org/10.1016/j.biortech.2020.124063

Cao Y, Wang L, Kang X, Song J, Guo H, Zhang Q (2023) Insight into atrazine removal by fallen leaf biochar prepared at different pyrolysis temperatures: batch experiments, column adsorption and DFT calculations. Environ Pollut 317:120832. https://doi.org/10.1016/j.envpol.2022.120832

Chen H, Gao Y, Li J, Fang Z, Bolan N, Bhatnagar A, Gao B, Hou D, Wang S, Song H, Yang X, Shaheen SM, Meng J, Chen W, Rinklebe J, Wang H (2022a) Engineered biochar for environmental decontamination in aquatic and soil systems: a review. Carbon Res 1:4. https://doi.org/10.1007/s44246-022-00005-5

Chen Z, Wei W, Chen H (2022b) Recent advances in waste—derived functional materials for wastewater remediation. EEH 1:86–104. https://doi.org/10.1016/j.eehl.2022.05.001

Contreras-García J, Johnson ER, Keinan S, Chaudret R, Piquemal J-P, Beratan DN, Yang W (2011) NCIPLOT: a program for plotting noncovalent interaction regions. J Chem Theory Comput 7:625–632. https://doi.org/10.1021/ct100641a

Deng J, Li X, Liu Y, Zeng G, Liang J, Song B, Wei X (2018) Alginate—modified biochar derived from Ca(II)—impregnated biomass: Excellent anti—interference ability for Pb(II) removal. Ecotox Environ Safe 165:211–218. https://doi.org/10.1016/j.ecoenv.2018.09.013

Deng W, Zhang D, Zheng X, Ye X, Niu X, Lin Z, Fu M, Zhou S (2021) Adsorption recovery of phosphate from waste streams by Ca/Mg—biochar synthesis from marble waste, calcium—rich sepiolite and bagasse. J Clean Prod 288:125638. https://doi.org/10.1016/j.jclepro.2020.125638

Dong J, Shen L, Shan S, Liu W, Qi Z, Liu C, Gao X (2022) Optimizing magnetic functionalization conditions for efficient preparation of magnetic biochar and adsorption of Pb(II) from aqueous solution. Sci Total Environ 806:151442. https://doi.org/10.1016/j.scitotenv.2021.151442

Du Z, Zheng T, Wang P, Hao L, Wang Y (2016) Fast microwave—assisted preparation of a low—cost and recyclable carboxyl modified lignocellulose—biomass jute fiber for enhanced heavy metal removal from water. Bioresour Technol 201:41–49. https://doi.org/10.1016/j.biortech.2015.11.009

Du Z, Zheng T, Wang P (2018) Experimental and modelling studies on fixed bed adsorption for Cu(II) removal from aqueous solution by carboxyl modified jute fiber. Powder Technol 338:952–959. https://doi.org/10.1016/j.powtec.2018.06.015

Du Z, Chen H, Guo X, Qin L, Lin D, Huo L, Yao Y, Zhang Z (2021) Mechanism and industrial application feasibility analysis on microwave—assisted rapid synthesis of amino—carboxyl functionalized cellulose for enhanced heavy metal removal. Chemosphere 268:128833. https://doi.org/10.1016/j.chemosphere.2020.128833

Fan Y, Wang H, Deng L, Wang Y, Kang D, Li C, Chen H (2020) Enhanced adsorption of Pb(II) by nitrogen and phosphorus co—doped biochar derived from Camellia oleifera shells. Environ Res 191:110030. https://doi.org/10.1016/j.envres.2020.110030

Feng M, Li M, Zhang L, Luo Y, Zhao D, Yuan M, Zhang K, Wang F (2022a) Oyster shell modified tobacco straw biochar: efficient phosphate adsorption at wide range of pH values. IJERPH 19:7227. https://doi.org/10.3390/ijerph19127227

Feng Z, Zhai X, Sun T (2022b) Sustainable and efficient removal of paraben, oxytetracycline and metronidazole using magnetic porous biochar composite prepared by one step pyrolysis. Sep Purif Technol 293:121120. https://doi.org/10.1016/j.seppur.2022.121120

Grimme S, Antony J, Ehrlich S, Krieg H (2010) A consistent and accurate *ab initio* parametrization of density functional dispersion correction (DFT—D) for the 94 elements H—Pu. J Chem Phys 132:154104. https://doi.org/10.1063/1.3382344

He Q, Luo Y, Feng Y, Xie K, Zhang K, Shen S, Luo Y, Wang F (2020) Biochar produced from tobacco stalks, eggshells, and Mg for phosphate adsorption from a wide range of pH aqueous solutions. Mater Res Express 7:115603. https://doi.org/10.1088/2053-1591/abcb3d

He R, Neupane M, Zia A, Huang X, Bowers C, Wang M, Lu J, Yang Y, Dong P (2022) Binder-Free wood converted carbon for enhanced water desalination performance. Adv Funct Mater 32:2208040. https://doi.org/10.1002/adfm.202208040

Jia X, Zhao X, Zhou Y, Li F, Liu W, Huang Y, Zhang H, Ma J, Hu G (2023) Tri–functional lanthanum–based biochar for efficient phosphorus recovery, bacterial inhibition, and soil fertility enhancement. Biochar 5:16. https://doi.org/10.1007/s42773-023-00216-y

Karunaratne TN, Nayanathara RMO, Navarathna CM, Rodrigo PM, Thirumalai RVKG, Pittman CU, Kim Y, Mlsna T, Zhang J, Zhang X (2022) Pyrolytic synthesis of graphene–encapsulated zero–valent iron nanoparticles supported on biochar for heavy metal removal. Biochar 4:70. https://doi.org/10.1007/s42773-022-00196-5

Li M, Luo Y, Zhao D, Qiu S, Zhang L, Zhang K, Song C, Wang F (2022a) Different La/Fe oxide composites for efficient phosphate removal from wastewater: Properties and mechanisms. J Environ Chem Eng 10:107329. https://doi.org/10.1016/j.jece.2022.107329

Li X, Huang Y, Liang X, Huang L, Wei L, Zheng X, Albert HA, Huang Q, Liu Z, Li Z (2022b) Characterization of biochars from woody agricultural wastes and sorption behavior comparison of cadmium and atrazine. Biochar 4:27. https://doi.org/10.1007/s42773-022-00132-7

Lian Q, Ahmad ZU, Gang DD, Zappi ME, Fortela DLB, Hernandez R (2020) The effects of carbon disulfide driven functionalization on graphene oxide for enhanced Pb(II) adsorption: investigation of adsorption mechanism. Chemosphere 248:126078. https://doi.org/10.1016/j.chemosphere.2020.126078

Liu B, Liu Z, Wu H, Pan S, Sun Y, Xu Y (2021) Insight into simultaneous selective removal of nitrogen and phosphorus species by lanthanum–modified porous polymer: performance, mechanism and application. Chem Eng J 415:129026. https://doi.org/10.1016/j.cej.2021.129026

Liu Z, Xu Z, Xu L, Buyong F, Chay TC, Li Z, Cai Y, Hu B, Zhu Y, Wang X (2022) Modified biochar: synthesis and mechanism for removal of environmental heavy metals. Carbon Res 1:8. https://doi.org/10.1007/s44246-022-00007-3

Liu B, Chen X, Huang N, Liu S, Wang Y, Lan X, Wei F, Wang T (2023a) Imaging the dynamic influence of functional groups on metal–organic frameworks. Nat Commun 14:4835. https://doi.org/10.1038/s41467-023-40590-6

Liu H, Lyczko N, Nzihou A, Eskicioglu C (2023b) Phosphorus recovery from municipal sludge–derived hydrochar: Insights into leaching mechanisms and hydroxyapatite synthesis. Water Res 241:120138. https://doi.org/10.1016/j.watres.2023.120138

Liu X, Yin H, Liu H, Cai Y, Qi X, Dang Z (2023c) Multicomponent adsorption of heavy metals onto biogenic hydroxyapatite: Surface functional groups and inorganic mineral facilitating stable adsorption of Pb(II). J Hazard Mater 443:130167. https://doi.org/10.1016/j.jhazmat.2022.130167

Lu T, Chen F (2012) Multiwfn: a multifunctional wavefunction analyzer. J Comput Chem 33:580–592. https://doi.org/10.1002/jcc.22885

Luo Y, Xie K, Feng Y, He Q, Zhang K, Shen S, Wang F (2021) Synthesis of a $La(OH)_3$ nanorod/walnut shell biochar composite for reclaiming phosphate from aqueous solutions. Colloid Surface A 610:125736. https://doi.org/10.1016/j.colsurfa.2020.125736

Luo M, Liu Q, Tao Y, Jiang X, Zang L, Yu H, Liu Y, Wang H, Niu Y, Niu Y (2024) Aging properties and cadmium remediation mechanism of biochar in sediment from phosphorus–rich water. J Hazard Mater 465:133062. https://doi.org/10.1016/j.jhazmat.2023.133062

Ma Y et al (2014) Polyethylenimine modified biochar adsorbent for hexavalent chromium removal from the aqueous solution. Bioresour Technol 169:403–408. https://doi.org/10.1016/j.biortech.2014.07.014

Marcińczyk M, Oleszczuk P (2022) Biochar and engineered biochar as slow—and controlled–release fertilizers. J Clean Prod 339:130685. https://doi.org/10.1016/j.jclepro.2022.130685

Qiu M, Liu L, Ling Q, Cai Y, Yu S, Wang S, Fu D, Hu B, Wang X (2022a) Biochar for the removal of contaminants from soil and water: a review. Biochar 4:19. https://doi.org/10.1007/s42773-022-00146-1

Qiu S, Zhao D, Feng Y, Li M, Liang X, Zhang L, Luo Y, Zhang K, Wang F (2022b) Adsorption performance and mechanism of Ca–Al–LDHs prepared by oyster shell and pop can for phosphate from aqueous solutions. J Environ Manage 303:114235. https://doi.org/10.1016/j.jenvman.2021.114235

Qu J, Yuan Y, Zhang X, Wang L, Tao Y, Jiang Z, Yu H, Dong M, Zhang Y (2022) Stabilization of lead and cadmium in soil by sulfur–iron functionalized biochar: Performance, mechanisms and microbial community evolution. J Hazard Mater 425:127876. https://doi.org/10.1016/j.jhazmat.2021.127876

Qu J, Du Z, Lei Y, Li M, Peng W, Wang M, Liu J, Hu Q, Wang L, Wang Y, Zhang Y (2023a) Microwave–assisted one–pot preparation of magnetic cactus–derived hydrochar for efficient removal of lead(II) and phenol from water: Performance and mechanism exploration. Bioresour Technol 388:129789. https://doi.org/10.1016/j.biortech.2023.129789

Qu J, Li Z, Wu Z, Bi F, Wei S, Dong M, Hu Q, Wang Y, Yu H, Zhang Y (2023b) Cyclodextrin–functionalized magnetic alginate microspheres for synchronous removal of lead and bisphenol a from contaminated soil. Chem Eng J 461:142079. https://doi.org/10.1016/j.cej.2023.142079

Shao P, Chang Z, Li M, Lu X, Jiang W, Zhang K, Luo X, Yang L (2023) Mixed–valence molybdenum oxide as a recyclable sorbent for silver removal and recovery from wastewater. Nat Commun 14:1365. https://doi.org/10.1038/s41467-023-37143-2

Sun T, Sun Y, Xu Y, Wang L, Liang X (2023) Effective removal of Hg^{2+} and Cd^{2+} in aqueous systems by Fe–Mn oxide modified biochar: a combined experimental and DFT calculation. Desalination 549:116306. https://doi.org/10.1016/j.desal.2022.116306

Tan Y, Zou Z, Qu J, Ren J, Wu C, Xu Z (2021) Mechanochemical conversion of chrysotile asbestos tailing into struvite for full elements utilization as citric–acid soluble fertilizer. J Clean Prod 283:124637. https://doi.org/10.1016/j.jclepro.2020.124637

Wadhawan S, Jain A, Nayyar J, Mehta SK (2020) Role of nanomaterials as adsorbents in heavy metal ion removal from waste water: A review. J Water Process Eng 33:101038. https://doi.org/10.1016/j.jwpe.2019.101038

Wang B, Ma Y, Lee X, Wu P, Liu F, Zhang X, Li L, Chen M (2021) Environmental–friendly coal gangue–biochar composites reclaiming phosphate from water as a slow–release fertilizer. Sci Total Environ 758:143664. https://doi.org/10.1016/j.scitotenv.2020.143664

Wang X, Wei-Chung Chang V, Li Z, Song Y, Li C, Wang Y (2022) Co–pyrolysis of sewage sludge and food waste digestate to synergistically improve biochar characteristics and heavy metals immobilization. Waste Manag 141:231–239. https://doi.org/10.1016/j.wasman.2022.02.001

Xia Y, Li Y, Sun Y, Miao W, Liu Z (2021) Co–pyrolysis of corn stover with industrial coal ash for in situ efficient remediation of heavy metals in multi–polluted soil. Environ Pollut 289:117840. https://doi.org/10.1016/j.envpol.2021.117840

Xu Y, Bai T, Li Q, Yang H, Yan Y, Sarkar B, Lam SS, Bolan N (2021a) Influence of pyrolysis temperature on the characteristics and lead(II) adsorption capacity of phosphorus–engineered poplar sawdust biochar. J Anal Appl Pyrol 154:105010. https://doi.org/10.1016/j.jaap.2020.105010

Xu Z, Gu S, Rana D, Matsuura T, Lan CQ (2021b) Chemical precipitation enabled UF and MF filtration for lead removal. J Water Process Eng 41:101987. https://doi.org/10.1016/j.jwpe.2021.101987

Yang S, Wen Q, Chen Z (2021) Effect of KH_2PO^{4-}–modified biochar on immobilization of Cr, Cu, Pb, Zn and as during anaerobic digestion of swine manure. Bioresour Technol 339:125570. https://doi.org/10.1016/j.biortech.2021.125570

Yang M, Wang H, Zuo JY, Deng C, Liu B, Chai L, Li K, Xiao H, Xiao P, Wang X, Chen W, Peng X, Han Y, Huang Z, Dong B, Sun C, Chen G (2022) Efficient separation of butane isomers via ZIF–8 slurry on laboratory– and pilot–scale. Nat Commun 13:4792. https://doi.org/10.1038/s41467-022-32418-6

Yuan S, Hong M, Li H, Ye Z, Gong H, Zhang J, Huang Q, Tan Z (2020) Contributions and mechanisms of components in modified biochar to adsorb cadmium in aqueous solution. Sci Total Environ 733:139320. https://doi.org/10.1016/j.scitotenv.2020.139320

Yun X, Ma Y, Zheng H, Zhang Y, Cui B, Xing B (2022) Pb(II) adsorption by biochar from co–pyrolysis of corn stalks and alkali–fused fly ash. Biochar 4:66. https://doi.org/10.1007/s42773-022-00189-4

Zhai M, Fu B, Zhai Y, Wang W, Maroney A, Keller AA, Wang H (2023) Simultaneous removal of pharmaceuticals and heavy metals from aqueous phase via adsorptive strategy: a critical review. Water Res 236:119924. https://doi.org/10.1016/j.watres.2023.119924

Zhang L, Liu Y, Wang Y, Li X, Wang Y (2021) Investigation of phosphate removal mechanisms by a lanthanum hydroxide adsorbent using p–XRD. FTIR and XPS Appl Surf Sci 557:149838. https://doi.org/10.1016/j.apsusc.2021.149838

Zhu X, Xiang Q, Chen L, Chen J, Wang L, Jiang N, Hao X, Zhang H, Wang X, Li Y, Omer R, Zhang L, Wang Y, Zhuang Y, Huang J (2024) Engineered Bacillus subtilis Biofilm@Biochar living materials for in–situ sensing and bioremediation of heavy metal ions pollution. J Hazard Mater 465:133119. https://doi.org/10.1016/j.jhazmat.2023.133119